GA–A26094

A CORRELATION ELECTRON CYCLOTRON EMISSION DIAGNOSTIC AND THE IMPORTANCE OF MULTI-FIELD FLUCTUATION MEASUREMENTS FOR TESTING NONLINEAR GYROKINETIC TURBULENCE SIMULATIONS

by
A.E. WHITE, L. SCHMITZ, W.A. PEEBLES, T.A. CARTER, T.L. RHODES, E.J. DOYLE, P.A. GOURDAIN, J.C. HILLESHEIM, G. WANG, C. HOLLAND, G.R. TYNAN, M.E. AUSTIN, G.R. McKEE, M.W. SHAFER, K.H. BURRELL, J. CANDY, J.C. DeBOO, R. PRATER, G.M. STAEBLER, R.E. WALTZ, M.A. MAKOWSKI, and the DIII-D TEAM

MAY 2008

GENERAL ATOMICS

DISCLAIMER

GA–A26094

A CORRELATION ELECTRON CYCLOTRON EMISSION DIAGNOSTIC AND THE IMPORTANCE OF MULTI-FIELD FLUCTUATION MEASUREMENTS FOR TESTING NONLINEAR GYROKINETIC TURBULENCE SIMULATIONS

by

A.E. WHITE,* L. SCHMITZ,* W.A. PEEBLES,* T.A. CARTER,* T.L. RHODES,* E.J. DOYLE,* P.A. GOURDAIN,* J.C. HILLESHEIM,* G. WANG,* C. HOLLAND,† G.R. TYNAN,† M.E. AUSTIN,‡ G.R. McKEE,# M.W. SHAFER,# K.H. BURRELL, J. CANDY, J.C. DeBOO, R. PRATER, G.M. STAEBLER, R.E. WALTZ, M.A. MAKOWSKI,§ and the DIII-D TEAM

This is a preprint of an invited paper to be presented at the Seventeenth Topical Conference on High Temperature Plasma Diagnostics, May 11-15, 2008, in Albuquerque, New Mexico, and to be published in the *Proceedings.*

*University of California, Los Angeles, California.
†University of California-San Diego, La Jolla, California.
‡University of Texas-Austin, Austin, Texas.
#University of Wisconsin-Madison, Madison, Wisconsin.
§Lawrence Livermore National Laboratory, Livermore, California.

Work supported by
the U.S. Department of Energy under DE-FG03-91ER54615, JP333701, DE-FG02-89ER53296, DE-FG02-07ER54917, DE-FG03-97ER54415, DE-FG02-89ER53296, DE-FC02-04ER54698, and DE-AC52-07NA27344

GENERAL ATOMICS ATOMICS PROJECT 30200
MAY 2008

GENERAL ATOMICS

Abstract

A correlation electron cyclotron emission (CECE) diagnostic has been used to measure local, turbulent fluctuations of the electron temperature in the core of DIII-D plasmas. This paper describes the hardware and testing of the CECE diagnostic and highlights the importance of measurements of multi-field fluctuation profiles for the testing and validation of nonlinear gyrokinetic codes. The process of testing and validating such codes is critical for extrapolation to next-step fusion devices. For the first time, the radial profiles of electron temperature and density fluctuations are compared to nonlinear gyrokinetic simulations. The CECE diagnostic at DIII-D uses correlation radiometry to measure the rms amplitude and spectrum of the electron temperature fluctuations. Gaussian optics are used to produce a poloidal spot size with $w_o \sim 1.75$ cm in the plasma. The intermediate frequency filters and the natural line width of the EC emission determine the radial resolution of the CECE diagnostic, which can be less than 1 cm. Wavenumbers resolved by the CECE diagnostic are $k_\theta \leq 1.8$ cm^{-1} and $k_r \leq 4$ cm^{-1}, relevant for studies of long-wavelength turbulence associated with the trapped electron mode and the ion temperature gradient mode. In neutral beam heated L-mode plasmas, core electron temperature fluctuations in the region $0.5 < r/a < 0.9$ increase with radius from ~0.5% to ~2%, similar to density fluctuations that are measured simultaneously with beam emission spectroscopy. After incorporating "synthetic diagnostics" to effectively filter the code output, the simulations reproduce the characteristics of the turbulence and transport at one radial location $r/a = 0.5$, but not at a second location, $r/a = 0.75$. These results illustrate that measurements of the profiles of multiple fluctuating fields can provide a significant constraint on the turbulence models employed by the code.

I. INTRODUCTION AND MOTIVATION

The cross-magnetic field transport of particles and energy in tokamak plasmas is larger than expected based on neoclassical theory and is believed to be due in large part to the transport of particles and energy caused by micro-instabilities or turbulence [1]. Multi-field fluctuation measurements as well as measurements of the plasma profiles and gradients are crucial for understanding the physics of cross-field particle, heat and momentum transport in the tokamak. The uncertainties involved in the measurement of the plasma profiles can often be a limiting factor in the testing and validation of advanced nonlinear gyrokinetic codes. This is because the turbulence driven transport predicted by these codes is found to be highly sensitive to the input values of the plasma profile gradients. The comparison between the profiles of two fluctuating fields and turbulence codes provides an important constraint because fixed gradient, local (flux-tube) simulation results for transport and fluctuation levels of one field at one radial location can often be brought into better agreement with the experimental values by changing the input gradient of the ion temperature within the experimental error bars [2].

An experiment with the specific goal of measuring the profiles of the fluctuations in two fields (density and electron temperature) for comparison with the nonlinear turbulence simulation code GYRO [3] was performed at DIII-D [4]. A new correlation electron cyclotron emission (CECE) diagnostic is used for measuring turbulent fluctuations of the electron temperature in the experiment. The local density fluctuations, measured with the beam emission spectroscopy (BES) diagnostic [5] are compared with the measured temperature fluctuations. Tests and characterizations of the new DIII-D correlation electron cyclotron emission (CECE) diagnostic are described in this article. The synthetic CECE diagnostic that is applied to GYRO output is also described.

II. THE CORRELATION ELECTRON CYCLOTRON EMISSION DIAGNOSTIC

The detection of electron cyclotron emission (ECE) is a standard technique used on tokamaks for determining the electron temperature profile [6]. When detecting ECE at the midplane on the low field side of the tokamak plasma cross-section with the angle of view roughly perpendicular to the total magnetic field direction, the effective radiation temperature measured with an ECE X-mode radiometer can be confidently identified with the perpendicular electron temperature in the limit that the ECE resonance layer is in an optically thick region of plasma that is in local thermal equilibrium [6-8]. However, for a single ECE radiometer signal there is an inherent limitation on the lowest level amplitude change that can be detected [7]. The sensitivity limit (set by the thermal noise level) can be improved by cross correlating two radiometer channels that have uncorrelated thermal noise. The method used in the CECE diagnostic at DIII-D relies on the spectral decorrelation properties of the thermal EC emission, which means that the thermal noise components of the two channels will be completely incoherent if the signals originate from different frequency bands [9]. The two channels are cross-correlated in order to extract the rms amplitude and power spectrum temperature fluctuations associated with turbulence. With this method, the sensitivity to low amplitude, broadband fluctuations is given as

$$\left(\tilde{T}_e^{\min}/T_e\right)^2 > \left(B_{vid}/B_{if}\right)/\sqrt{N} \quad , \tag{1}$$

where $N = 2\ B_{vid}\ \Delta t$ is the number of independent samples used to determine the correlation function [9-11]. The sensitivity also improves when the bandwidth of the signal of interest is less than the video bandwidth, $B_{sig} < B_{vid}$ [12]. By averaging over long data records, $\Delta t =$ 400 ms, the sensitivity of the correlation ECE diagnostic approaches $T_e/T_e \approx 0.2\%$, with $B_{sig} =$ 400 kHz, $B_{if} =$ 110 MHz and $N = 2\ B_{vid} \cdot \Delta t$ used in equation (3). When the IF filters do not overlap in frequency, the cross-correlation coefficient at zero time delay is directly related to the normalized radiation temperature fluctuation amplitude [13]. The rms amplitude can also be obtained by integrating the cross-power spectrum over the frequency range of interest [9].

Correlation radiometry of ECE to measure electron temperature turbulence was first performed in the advanced stellarator Wendelstein-7 (W7-AS) [13] and in the Texas Experimental Tokamak (TEXT) [9]. Correlation ECE systems have since been

implemented on several other tokamaks [14-16]. For a review of past correlation ECE measurements see the review by Watts [17] and references therein.

III. CORRELATION ELECTRON CYCLOTRON EMISSION AT DIII-D, SYSTEM OVERVIEW

A correlation ECE (CECE) diagnostic is used on DIII-D to measure long-wavelength electron temperature fluctuations ($k_\theta < 1.8$ cm^{-1}, $k_r < 4$ cm^{-1}). A four-channel heterodyne correlation radiometer receives 2nd harmonic X-mode cyclotron emission with a single line of sight, as shown in figure 1. A parabolic mirror with focal length f = 84 cm is located inside the vacuum and collects radiation from the plasma. The parabolic mirror forms a Gaussian beam with beam waist $2\omega_0 \sim 3.5$ cm near half radius. The angle of the parabolic mirror relative to the midplane can be varied between 7 and 15 degrees. The emerging collimated radiation is then coupled to a flat mirror and then onto an aspherical, high-density polyethylene dielectric lens with focal length f = 27 cm. The focused beam is coupled to a dual-mode horn antenna [18].

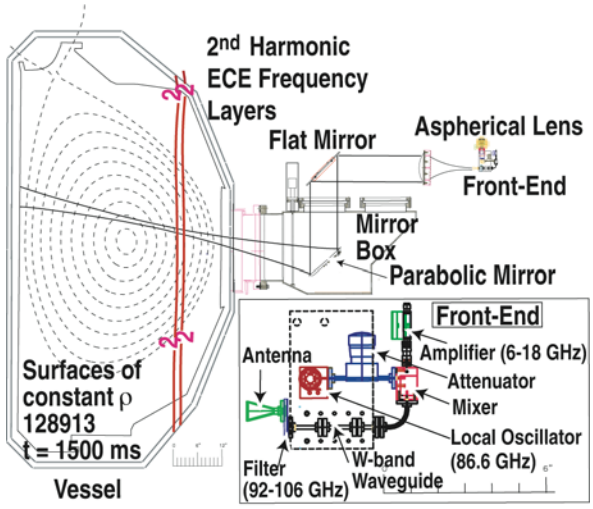

FIG. 1. (Color online) The focusing optics used in the CECE system (not to scale) is shown with the vacuum vessel and surfaces of constant ψ from a L-mode plasma, discharge 128913, t = 1500 ms. A parabolic mirror (f = 84 cm) couples radiation from two closely spaced, radially separated sample volumes in the plasma to the CECE radiometer. The beam waist ($1/e^2$ power diameter) is 3.5 cm near half radius. The angle of the parabolic mirror with respect to the vessel midplane is adjustable between 7 and 15 degrees. An HDPE aspherical lens (f = 27 cm) is used with a dual-mode horn antenna.

A block diagram of the microwave circuit of the CECE diagnostic is shown in figure 2. A mechanically tuned, variable frequency Gunn oscillator (tuned for 86.6 GHz) is used as the local oscillator (LO). After the antenna, only the upper side band frequency range 92-106 GHz is admitted to the mixer using a strip-line bandpass filter. The local oscillator power is attenuated to obtain the correct LO power to the mixer. After down-

conversion in the mixer, the signal is passed to the first power amplifier (range 6-18 GHz, gain +30 dB).

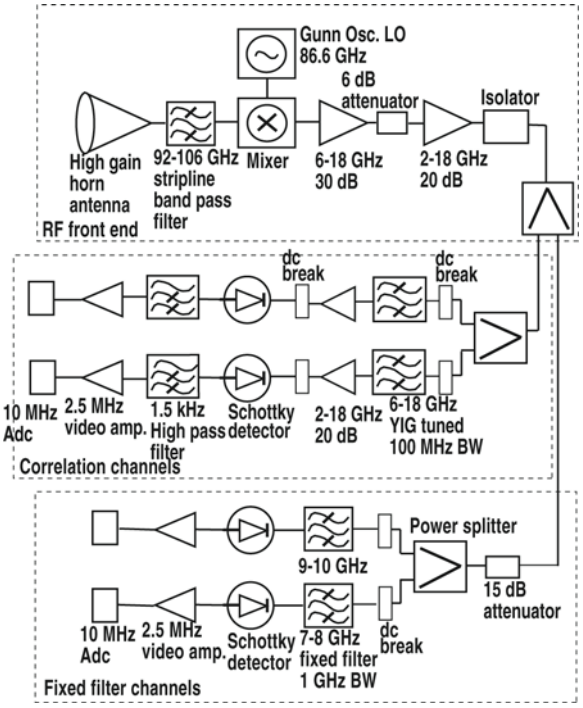

FIG. 2. Block-diagram of CECE system circuit elements showing the two IF sections, with correlation channels and fixed filter channels. The correlation channels use two narrow band (-3 dB bandwidth, 110 MHz) remotely tunable YIG filters as intermediate frequency filters.

The conversion loss of the mixer (-9 dB) and the loss in the waveguide sections (-2 dB) are measured in the laboratory. Losses from the quartz window, antenna and bandpass filters are estimated at -3.5 dB. The total loss before the first power amplifier is approximately -14.5 dB. After the first power amplifier, the CECE signal is transferred to the receiver box using a low-loss (~4 dBm over the range 6-18 GHz) six foot length of sma cable. The signal is typically attenuated -6 dB before being amplified +20 dB by a 2-18 GHz microwave amplifier. After this second amplifier the signal is split and fed to two IF sections.

The first IF section shown in figure 2 contains the narrow-band IF filters used for fluctuation measurements. These are Watkins Johnson Compact Yttrium Iron Garnet (YIG) filters, which are current-tunable between 6-18 GHz. The YIG filters have a -3 dB pass-band, B_{IF} = 110-118 MHz across the tunable center frequency range of 6-17.6 GHz. The tuning currents of the YIG filters are remotely controlled and monitored so that the radial positions of the observed emission volumes can be actively altered during a shot or on a shot-to-shot basis. The signals are amplified after the YIGs using

+20 dB microwave amplifiers before rectification/integration using Schottky diode detectors. Inner and outer dc breaks are used before and after the detectors and do not alter the frequency response of the system in the range of microwave frequencies considered here. The dc breaks isolate the ground plane of the IF section from the machine ground or digitizer ground planes, eliminating dc contact potentials and ground loops. The signals emerging from the detectors are passively high-pass filtered at 1.5 kHz before the video amplifier (analog bandwidth 5.0 MHz). Amplifying only the ac portion of the signals improves the sensitivity of the measurement to low amplitude temperature fluctuations because the full dynamic ranges of the video amplifier and the digitizer can be used to measure only the 10-50 eV fluctuating portion of the signal, rather than both the dc 1-4 keV equilibrium temperature and the fluctuating signal combined. The signals do not need to be absolutely calibrated to measure the relative fluctuation level, $\tilde{T}_e/T_e$ [9,13].

The second IF section, figure 2, contains the wideband (Δf = 1 GHz) fixed filters with frequencies 9-10 GHz and 7-8 GHz. Shottky detectors are used for these channels as well. These channels are not high-pass filtered and are used to measure the local electron temperature for comparison and/or reference to the DIII-D 40-channel ECE radiometer [19].

After the video amplifiers the four rectified CECE signals are sent via low-loss coaxial cables from the tokamak test cell to the data acquisition area. All four channels are low-pass filtered at 2.5 MHz using passive filters and digitized using 12 bit digitizers with a sampling rate of 10 MHz. A digital low-pass filter is typically applied subsequently to the correlation channels resulting in an effective video bandwidth, B_{vid} = 1 MHz during data analysis to improve the sensitivity [13].

IV. TESTS AND CHARACTERIZATION OF THE CECE DIAGNOSTIC

A. Beam Waist Measurements

The poloidal spatial resolution of the CECE system is determined by the $1/e^2$ power diameter, 2ω, of the Gaussian antenna pattern. The antenna pattern is measured in the laboratory. A probe beam of 94 GHz is launched from the dual mode antenna and is focused using an optical arrangement identical to that used at DIII-D. The beam spatial profile at many locations along the beam path is measured with a power meter on a translation stage. The data for the antenna pattern in the E-field plane at three locations (corresponding to three major radii at DIII-D) are shown in figure 3(a) R = 222 cm (b) R = 209 cm (c) R = 197 cm, are shown. Data have been fit with Gaussian curves (red solid lines). The beam diameters ($1/e^2$ power diameter) are obtained from the fits. The uncertainty in the measurements is estimated to be ±0.2 cm. The beam waist is $2\omega_0$ = 3.5 cm near R = 209 cm, giving a poloidal wavenumber range of $k_\theta < 2\pi/2\omega_0 = 1.8$ cm^{-1}.

B. Calibration of the CECE Radiometer

The CECE IF section is calibrated using a 2-18 GHz excess noise ratio (ENR) calibrated noise source in place of the mixer in the microwave circuit. The signal with and without the noise source powered on is fed to the first amplifier and the dc responses of the four channels are recorded. In order to estimate the calibration factor needed to convert Volts to eV when viewing the plasma, the front-end losses must be taken into account to obtain the estimated calibration factor for the entire CECE system. The comparison of the temperature measured with the calibrated CECE radiometer (red, dashed line) and the standard 40-channel ECE radiometer [19] (black, solid line) from 127714 t = 0-4000 ms are shown in figure 4. The temperature measured at t = 3200-3300 ms at 96.1 GHz with the CECE system is 1.2±0.2 keV. This value is in good agreement with temperature measured with the standard 40 channel ECE, where T_e = 1.185 keV at 96.5 GHz, t = 3250 ms. The temperature measured with the CECE radiometer is typically within 10%-20% of the value obtained with the 40-channel radiometer.

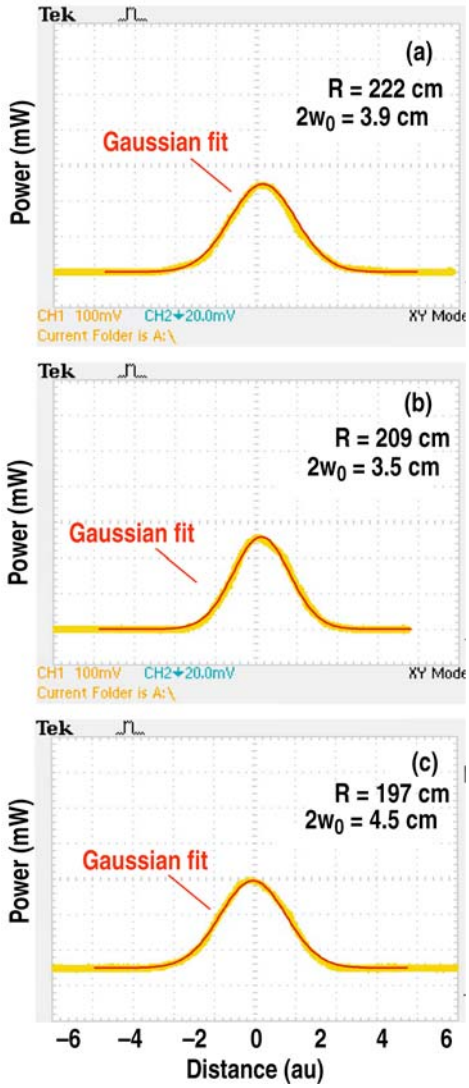

FIG. 3. The measured power profiles of the CECE antenna pattern in the E-field plane at three radial locations are shown. (a) R = 222 cm (b) R = 209 cm (c) R = 197 cm. The antenna pattern data has been fit with Gaussian curves. The beam diameters ($1/e^2$ power diameter) are obtained from the fits. The beam waist ($2w_o$ = 3.5 cm) is located at R = 209 cm, near mid-radius ($r/a \sim 0.5$) in a typical L-mode plasma.

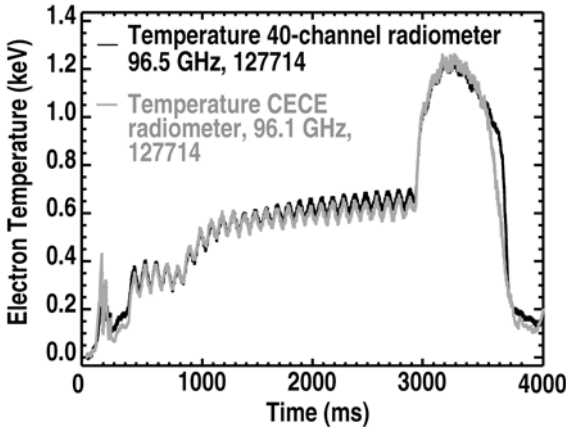

FIG. 4. Comparison between the electron temperature at $r/a \sim 0.6$ measured with the CECE diagnostic and the standard 40 channel radiometer. The temperature from the 40-channel radiometer at 96.5 GHz is the black solid line and the temperature from the CECE fixed filter channel at 96.1 GHz is the red-dashed line. The CECE signal is smoothed over 0.1 ms and the offset of the digitizer is corrected by adding 0.055 V. The calibration factor 3.8 keV/V (determined using a noise source to measure the sensitivity of the CECE IF sections and correcting for front-end losses) has been multiplied by the CECE fixed filter signal to obtain the measured temperature in units of keV.

C. Refractive Effects

The effects of refraction will become increasingly important as the cutoff density is approached when the frequency of the right hand wave becomes equal to the frequency of 2nd harmonic cyclotron emission, $f_{RH} = 2f_{EC}$. Refractive effects on the CECE signals are estimated using the ray tracing code GENRAY [20]. GENRAY is used to launch rays from the top, center, and bottom of a 25 cm disk from the location of the parabolic mirror at an angle of 7 degrees with respect to the midplane [figure 5(a)] for 128913 at $t =$ 1500 ms. The seven rays are focused to a second disk in the plasma with diameter 3.8 cm. Figure 5(b) shows these rays (solid blue lines) compared with straight-line paths (red dashed lines). The estimated effects of refraction are a shift of the sample volume up vertically by roughly 0.4 cm and a change in diameter of 2-3 mm.

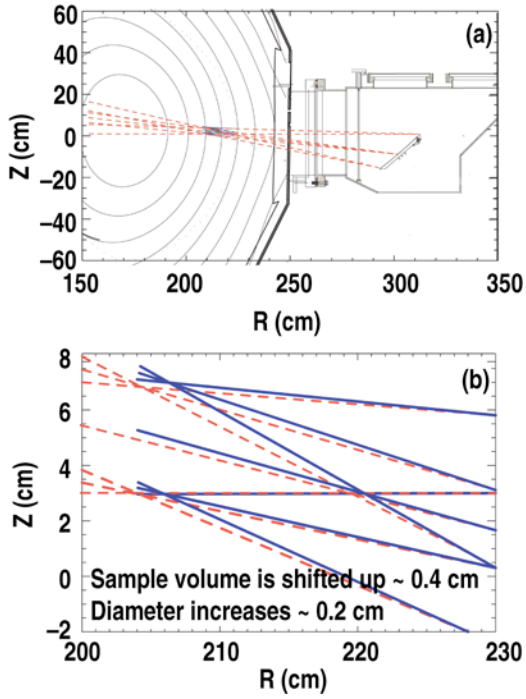

FIG. 5. (a) The ray-tracing code GENRAY is used to launch rays from the top, center, and bottom of a 25 cm disk from the location of the parabolic mirror at an angle of 7 degrees with respect to the midplane. The rays are focused to a second disk in the plasma with diameter 3.8 cm (determined by laboratory measurements of the antenna pattern). (b) The deviation of the top and bottom rays (solid colored lines) from the parallel lines is due to refraction. The main effect of refraction is to shift the sample volume up vertically by 0.4 cm. The perturbation to the beam waist at $R \sim 204$ cm is a change in diameter of <0.2 cm, which is less than the estimated uncertainty in the measurement of the antenna pattern.

D. Radial Resolution of the CECE Diagnostic

The extent of the radial sample volume for the CECE diagnostic is dominated by the natural line width of the EC emission layer and can be estimated using calculations of the emissivity. Figure 6(a) shows the calculated emissivity for a single frequency in the L-mode plasma 128913 $t = 1500$ ms. The emissivity is $G(s) = I(s)\alpha(s)e^{-\tau(s)}$ where $\alpha(s)$ is the absorption coefficient along the line of sight, s, and $\tau(s)$ is the optical depth [21]. Figure 6(b) shows the integral of the emissivity. The natural line width of a single frequency is calculated as the distance between the radii where 5% and 95% of the cyclotron emission power escapes in figure 6(b) and is ~0.73 cm for 128913 at $t = 1500$ ms for 93.6 GHz. The sum of emissivities for five frequencies between 93.6 and 93.71 GHz is shown in figure 6(c). This is used to estimate the radial extent of the sample volume for a single YIG signal, which is estimated to be ~0.98 cm in 128913 at $t = 1500$ ms. The radial overlap of the two sample volumes (YIG 1 shown in

black, YIG 2 shown in red) is shown in figure 6(d) for a typical case. When the YIG filters are set 200 MHz apart the sample volumes are separated center to center by ~0.4 cm in 128913, t = 1500 ms. Based on the radial extent of both sample volumes, the width used to estimate the radial wavenumber range, $k_r = 2\pi/d < 4$ cm^{-1}, is d =1.5 cm.

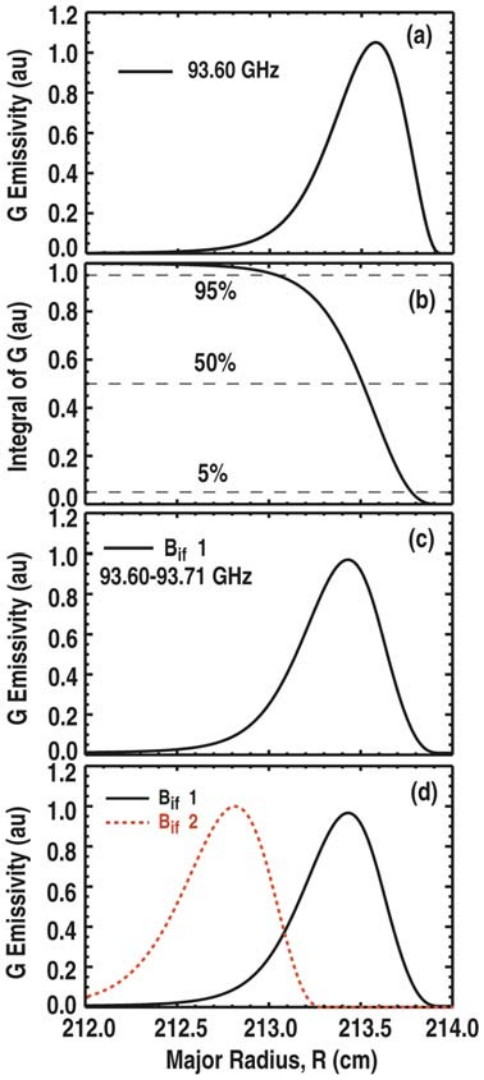

FIG. 6. (Color online) Part (a) shows the calculated emissivity of a single frequency, 93.6, from 2nd harmonic X-mode emission in the L-mode plasma 128913 t = 1500 ms. Part (b) shows the integral of the emissivity. The natural line width of a single frequency is calculated from as the distance between the radii where 5% and 95% of the power escapes. The natural line width in 128913 at t = 1500 ms is ~0.73 cm for 93.6 GHz. The combined emissivities of all frequencies selected by the YIG filter in the -3 dB bandwidth (93.6-93.71 GHz) are shown in part (c). This defines the effective width of the YIG filter, as calculated as the radial distance between the 5% power point in the integral of the emissivity for 93.6 GHz and the 95% point for 93.71 GHz. The effective width of the YIG filter defines the radial extent of the sample volume and is ~0.98 cm in this L-mode plasma. The radial overlap of the sample volumes (YIG 1 shown in black, YIG 2 shown in red) is shown in part (d) for a typical case where the YIG filters are set 200 MHz apart.

E. Characterizing Electronics Noise and Finite Filter Overlap

Sources of spurious correlations (not real $\tilde{T}_e$) can include real effects in the plasma such as fluctuations in density or index of refraction or magnetic flutter [22]. For the L-mode plasmas of interest these are estimated to be negligible. Other sources of spurious correlation may include non-plasma effects such as finite filter overlap or harmonics in the nonlinear microwave circuit elements such as amplifiers or mixers.

Spurious correlations in the electronics can be identified by calculating the cross-correlation between channels when there is no plasma present. The digitizers are triggered -50 ms before the plasma breaks down on every discharge. Any features present in the cross-correlation between t = -50-0 ms would be the result of correlations in the electronics or microwave circuit. Figure 7 shows the cross-power spectrum averaged over the 50 ms before plasma breakdown (red line) in shot 125113 compared to the cross-power during L-mode (black line) from t = 700-750 ms when true temperature fluctuations (the features with f < 100 kHz) are measured. The features in the cross-power before the plasma breakdown are two to three orders of magnitude lower than the cross-power when plasma is present and will not contribute to the measured temperature fluctuations.

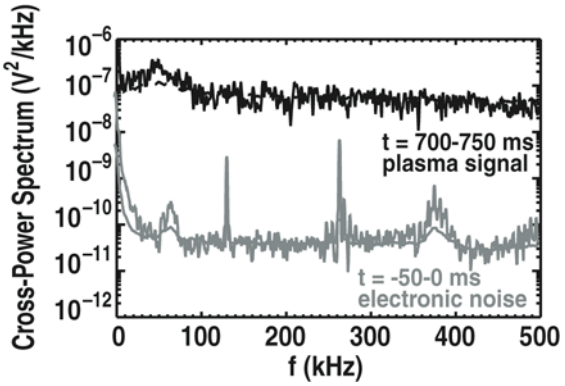

FIG. 7. The cross-power of temperature fluctuations (units V^2/kHz or T_e^2/kHz) is shown during an L-mode plasma 125113, t = 700-750 ms (black line). The cross-power of fluctuations in the system *before* the plasma breakdown in the same shot (t = -50-0 ms) is shown in red. The spurious correlations related to electronic noise are orders of magnitude below the real temperature fluctuation signal and the thermal noise level when plasma is present.

The effect of finite filter overlap is tested in a series of repeat, start-up L-mode plasmas (125113-125123) and the features that correspond to thermal noise and real temperature fluctuations can be distinguished from one other. Figure 8 shows

the cross-correlation functions R_{xy} in units $\left(\tilde{T}_e/T_e\right)^2$ and the cross-power spectra P_{xy} in units $\left(\tilde{T}_e/T_e\right)^2/\text{kHz}$ calculated at $r/a \sim 0.7$ for three different values of the YIG filter separation: figure 8(a,b) the YIG filters are separated (center to center) by ~50 MHz, figure 8(c,d) separated by ~70 MHz, and figure 8(e,f) separated by ~270 MHz. This allows for the identification of two features in the cross-correlation functions in (a) and (c). The narrow peak at zero-time delay in the correlation function, R_{xy}, is caused by finite-filter overlap and represents the amount of thermal noise that is common to both signals and is unrelated to the electron temperature turbulence. The width of this thermal noise peak is determined by $1/B_{vid}$, in this case B_{vid} = 2.5 MHz. The thermal noise extends up to B_{vid} and can be identified in the cross-power spectrum in figure 8(b) as an offset of the spectrum above the estimated spectral noise level (calculated as the square root of the variance of P_{xy}). As the filters are separated, the narrow feature in the cross-correlation function, R_{xy}, associated with the thermal noise seen in figure 8(a,c) is no longer seen in figure 8(e). As the filters are further separated, the offset in the cross-power caused by thermal noise will approach the spectral noise level, as seen in figure 8(d,f). The real temperature fluctuations, seen as the feature between ~20-100 kHz in the cross-power spectra, P_{xy}, and as the feature in R_{xy} marked by the horizontal dashed line, will remain correlated as the filters are separated. That the thermal noise decorrelates when the IF filters no longer overlap has also been tested using a W-band noise source in past work at DIII-D [28].

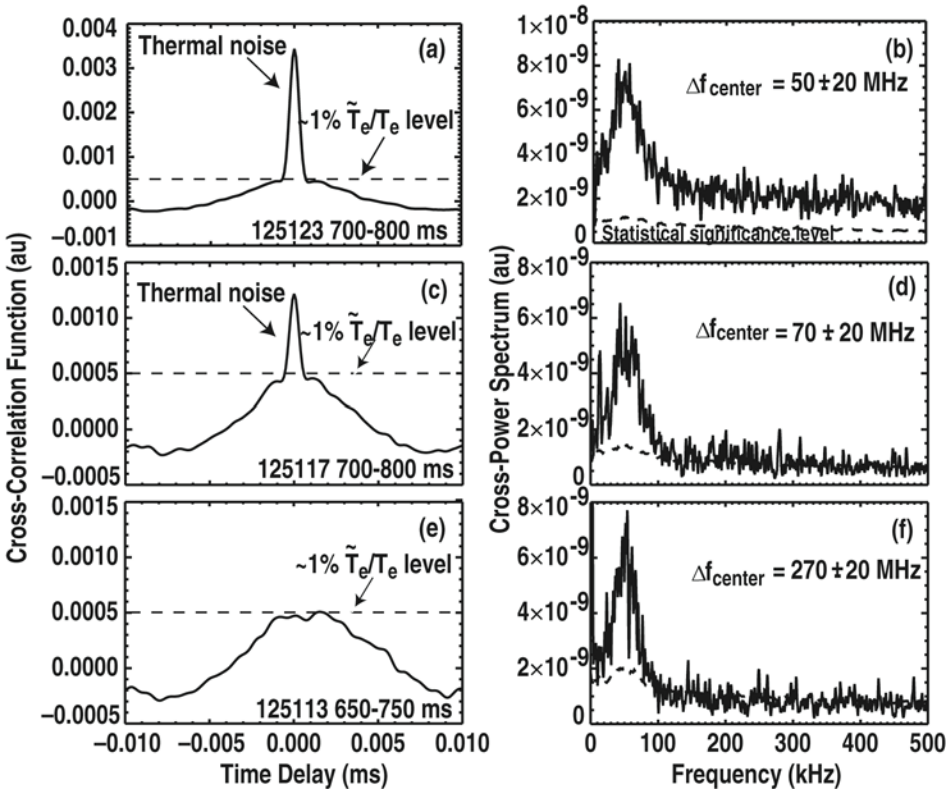

FIG. 8. The cross-correlation functions (R_{xy}) and the cross-power spectra (P_{xy}) pairs calculated at $r/a \sim 0.7$ are shown for three different values of the YIG filter separation: (a-b) the YIG filters are separated (center to center) by ~50 MHz, (c-d) ~70 MHz, and (e-f) ~270 MHz. As the filters are further separated, the narrow feature in the cross-correlation function, R_{xy}, associated with the thermal noise seen in (a) and (c) is no longer seen in (e). In contrast, the feature in R_{xy} associated with real temperature fluctuations remains correlated, with the temperature fluctuation level marked by the horizontal dashed line in (a,c,e). Similarly the real temperature fluctuations between ~20-100 kHz remain correlated in the cross-power spectra, P_{xy}, as the filters are separated. The thermal noise is broadband and can be identified in the cross-power spectrum in (b) as an offset of the spectrum above the estimated spectral noise level (calculated as the square root of the variance of P_{xy}). As the filters are further separated, the offset in the cross-power caused by thermal noise will approach the statistical noise level, as seen in (d) and (f).

V. CECE SYNTHETIC DIAGNOSTIC MODELING

In order to compare the measured electron temperature fluctuations with the nonlinear gyrokinetic transport code GYRO, a synthetic diagnostic that models the spatial sensitivity of the CECE system is used. One result of running nonlinear GYRO simulations is to produce real-space fluctuation fields, $\tilde{\phi}$, $\tilde{n}_e$, and $\tilde{T}_e$ in the (R,Z) plane where R is the major radius of the tokamak and Z is a generalized vertical coordinate. These components can be mapped to the field-line following coordinate system that is employed by GYRO. The color contours in figure 9(a,b) are the real-space fluctuation fields of electron temperature (a) and density fluctuations (b) calculated using GYRO. Synthetic diagnostics are used to filter the raw GYRO output to allow for direct comparison with the experiment [23]. A point-spread function, $\psi(R,Z)$, is used to calculate the synthetic fluctuation signal corresponding to a diagnostic centered at (R_0,Z_0) from the "unfiltered" real-space fluctuation fields using the following convolution [24]:

$$f_{\text{synthetic}}(R_0,Z_0,t) = \frac{\iint dRdZ\psi(R-R_0,Z-Z_0)\, f_{\text{sim}}(R,Z,t)}{\iint dRdZ\psi(R-R_0,Z-Z_0)} \quad . \tag{2}$$

The CECE point spread function (PSF) in figure 9(a) is shown above the midplane and the BES PSF in part (b) is shown below the midplane where the diagnostics are viewing the plasma in 128913 at t = 1500 ms.

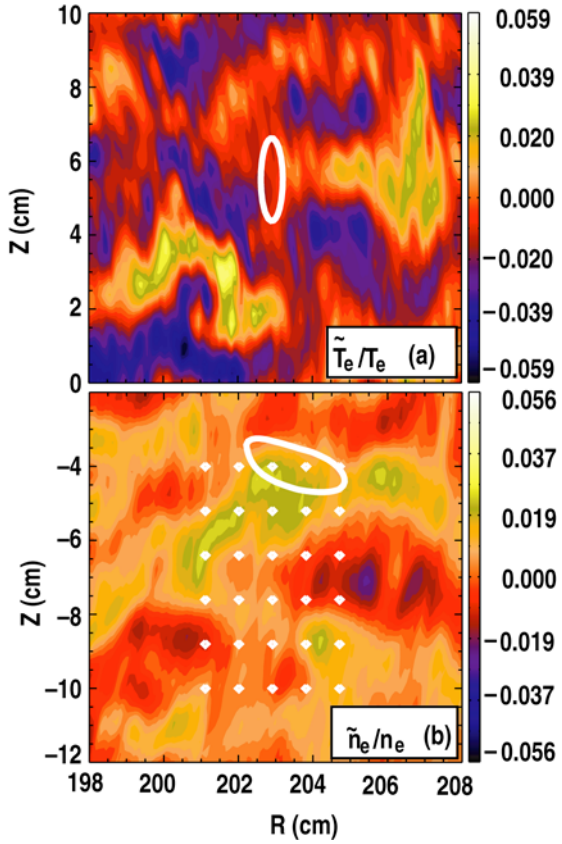

FIG. 9. The synthetic diagnostics use point-spread functions (PSFs) to model the sample volumes of the CECE and BES diagnostics. The CECE PSF (a) is shown above the midplane and the BES PSF (b) is shown below the midplane where the diagnostics are viewing the plasma in 128913 at t = 1500 ms. The color contours are the electron temperature (a) and density fluctuations (b) calculated using the GYRO code. The PSF for the CECE diagnostic is modeled using an asymmetric Gaussian. The $1/e^2$ power diameter in the vertical direction is 3.8 cm. The $1/e^2$ power diameter in the radial direction is 1 cm. The PSF of the BES diagnostic radial extent of ~2 cm and vertical extent of ~1.5 cm.

For the BES system, the PSF will include effects from the collection optics, sight-line geometry, neutral beam cross-section intensity and the finite atomic transition time of the collisionally excited beam atoms. Calculation of the PSF of the BES diagnostic at DIII-D is documented in reference [25]. The radial extent of the BES PSF used in this work is ~2 cm and the vertical extent is ~1.3 cm [25] and varies with radius and local plasma density.

For the CECE diagnostic, a model PSF is chosen as Gaussian in the vertical and radial directions [24]:

$$\psi_{\mathrm{CECE}} = \exp\left(-\frac{1}{2}\left[\left(\frac{R-R_0}{L_R}\right)^2 + \left(\frac{Z-Z_0}{L_Z}\right)^2\right]\right) \quad , \tag{3}$$

where $L_R = \Delta r/4$, and $L_Z = \Delta z/4$ cm. Here Δr is the calculated radial sample volume $1/e^2$ power diameter and Δz is the vertical sample volume $1/e^2$ power diameter.

Based on results of emissivity calculations summarized in figure 6, the $1/e^2$ power diameter of the Gaussian used to model the radial sample volume in 128913 at $t =$ 1500 ms is taken as $\Delta r =$ 1 cm. Based on the measurements of the antenna pattern, the $1/e^2$ diameter of the Gaussian used to model the vertical sample volume in the CECE PSF at $r/a = 0.5$ is $\Delta z =$ 3.8 cm. For the comparisons to GYRO presented in this work the CECE PSF does not yet include the effects of refraction and therefore is written as

$$\psi_{CECE} = \exp\left(-8\left[\left(\frac{R-R_0}{1\text{ cm}}\right)^2 + \left(\frac{Z-Z_0}{3.8\text{ cm}}\right)^2\right]\right) \quad , \tag{4}$$

With $Z = Z_0$, we find $\psi = 1/e^2$ at $R - R_0 =$ ±0.5 cm (giving the 1 cm radial diameter). Likewise, we obtain $\psi = 1/e^2$ with $Z - Z_0 =$ 1.9 cm for $R = R_0$ (giving the ~3.8 cm vertical diameter).

VI. COMPARISON BETWEEN THE PROFILES OF TEMPERATURE AND DENSITY FLUCTUATIONS AND NONLINEAR GYROKINETIC SIMULATIONS

A series of repeat DIII-D L-mode discharges (128915-128919, 128923) is used to scan the CECE and BES diagnostics simultaneously to measure the radial profiles of electron temperature and density fluctuations in an experiment specifically designed to facilitate comparisons with GYRO [26]. Both diagnostics are most sensitive to long-wavelength turbulence (CECE $k_\theta < 1.8$ cm^{-1}, $k_r < 4$ cm^{-1}, BES $k_\theta < 2$ cm^{-1} and $k_r < 3$ cm^{-1}) and *not* to very short wavelength turbulence. The CECE and BES diagnostics measure fluctuations simultaneously at the same radial location with the sample volumes vertically and toroidally separated.

In the present analysis, local turbulence and transport properties are modeled using two separate flux-tube simulations with GYRO, centered at $r/a = 0.5$ and $r/a = 0.75$. In order to assess how well GYRO models the turbulence characteristics, the PSFs for the synthetic diagnostics (section VI) are used to post-process the GYRO output. The color contours in figure 9(a,b) are the real-space fluctuation fields, in the (R,Z) plane, electron temperature (a) and density fluctuations (b), as calculated from GYRO. The PSF is used to calculate the synthetic fluctuation signal of a real diagnostic (centered at (R_0,Z_0) from the "unfiltered" real-space fluctuation fields. A time series for the fluctuations can be obtained from the fluctuation field at one point (R_0,Z_0). The simulated time series (the simulation time-step is C_s/a, where C_s is sound speed and a is minor radius) for density and temperature fluctuations are shown before and after the application of the PSF in figure 10. The "raw" GYRO time traces before the PSF is applied are shown in black. The GYRO time traces *after* the PSF is applied are shown in red. Because the PSFs model the spatial sensitivity of the diagnostics, and the effect of the finite sample volume is to attenuate higher frequency components, the red GYRO trace (PSF applied) compared to the black GYRO trace (no PSF applied) is much smoother. In general, the radial extent of the PSF tends to attenuate all frequencies (all wavenumbers) equally, whereas the poloidal extent of the PSF preferentially attenuates high frequency (high wavenumber) components [27]. Using GYRO results with the PSF applied standard data analysis procedures (e.g. autopower, cross-power, etc) are used to compare GYRO results to experimental results. In this work the autopower spectra of density fluctuations and temperature fluctuations are calculated and integrated in the frequency range (40-400 kHz) to obtain the fluctuation levels that are compared to the experimental results.

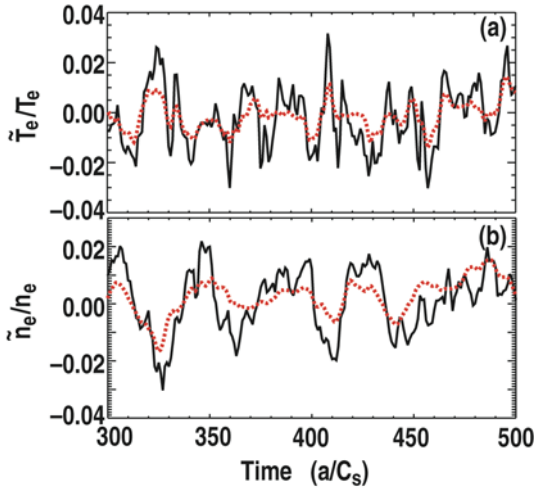

FIG. 10. A time series for density or temperature fluctuations can be obtained from GYRO results at one point (R_0, Z_0) in the fluctuation fields shown in figure 10(a,b). The "raw" time series (before using the PSF) are shown here shown in black. Temperature fluctuations are shown in part (a) and density fluctuations are shown in part (b). The red trace corresponds to the time series after applying the PSF. Higher frequencies are attenuated due to the spatial averaging of the diagnostics' sample volumes. The time series after applying synthetic diagnostics (red traces) are used in the calculation of auto power spectra or cross-power spectra for comparison with experimental measurements.

The fluctuation levels calculated using the GYRO results from local (flux-tube) fixed gradient simulations for reference discharge 128913 at $r/a = 0.5$ and $r/a = 0.75$ are shown along with the experimentally determined profiles in figure 11. The GYRO $\tilde{T}_e/T_e$ are shown as open circles, $\tilde{n}/n$ are shown as open squares. The fluctuation levels from GYRO are in good agreement at $r/a = 0.5$ (where transport levels predicted by GYRO are also in good agreement with the power balance calculations). At $r/a = 0.75$, the predicted fluctuation levels are less than the experimental levels. The difference in agreement between the experiment and the codes at the two radial locations highlights the importance of using profiles of fluctuations in testing the results of nonlinear gyrokinetic simulations.

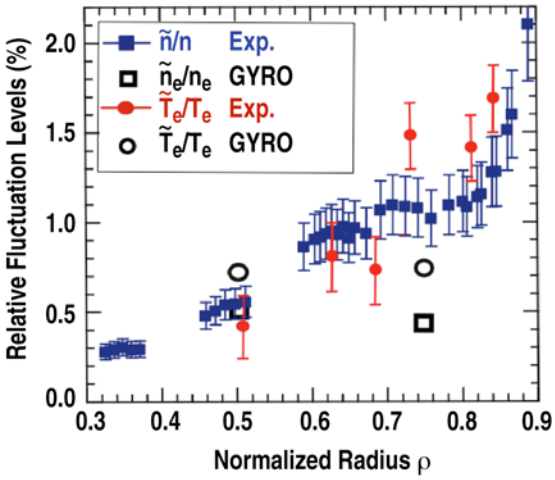

FIG. 11. A series of repeat L-mode discharges (128915-128919, 128923) is used to scan the CECE and BES diagnostics simultaneously to measure the radial profiles of electron temperature (red closed circles) and density fluctuations (blue closed squares). The fluctuation levels calculated using the GYRO results from local (flux-tube) fixed gradient simulations for reference discharge 128913 at $r/a = 0.5$ and $r/a = 0.75$ are shown. The GYRO T_e/T_e are open circles, n/n are open squares. The fluctuation levels from GYRO are in good agreement at $r/a = 0.5$. At $r/a = 0.75$, the fluctuation levels are less than the experimental levels.

VII. CONCLUSIONS

This paper has described a new Correlation ECE diagnostic (CECE) at DIII-D. Testing the diagnostic and the process of incorporating the test results into a synthetic diagnostic has been emphasized. In this work, the measured profiles of two fluctuating fields have been compared to results from the nonlinear gyrokinetic turbulence code GYRO. Such a comparison provides a constraint because, in general, fixed gradient, local (flux-tube) simulation results for transport and fluctuation levels at one radial location can often be brought into good agreement with the experimental values [2]. Performing more expensive simulations to include the high wavenumber (high-k) modes or using global simulations in order to capture non-local effects can in some cases bring improvement in the levels of agreement. However, for the case studied here, none of the above "expensive" updates to the simulations would fully resolve the discrepancy between the level of agreement at $r/a = 0.5$ and $r/a = 0.75$. Updates to the CECE synthetic diagnostic such as the ability to cross-correlate two synthetic CECE signals [24], and including the effects of refraction will improve the quantitative agreement between the experiment and the results of the local simulations at $r/a = 0.5$ but not at $r/a = 0.75$. The profile of the turbulence is therefore a significant constraint on the codes.

In general, the comparison we have done between the profiles of electron temperature fluctuations, density fluctuations and GYRO highlights the need to perform testing and validation studies that exploit the variety of different turbulence diagnostics available on a tokamak such as DIII-D. Dedicated experiments — designed with the comparison to nonlinear gyrokinetic codes as a primary goal — will need to be performed. New and upgraded diagnostics that measure multiple fluctuating fields at several spatial scales must be used to constrain the simulations so that uncertainties in experimental profiles and gradients will not dominate the trends in the results. Simulations (linear, nonlinear, and transport modeling) should be used in combination *prior to an experiment* to explore how different characteristics of the turbulence (e.g. high-k and low-k density fluctuations, temperature fluctuations, phase angle) respond in realistic experimental conditions.

References

[1] J. Wesson, *Tokamaks*, 3rd Ed. (Clarendon Press, Oxford, UK, 2004) pp. 150.
[2] J. Candy and R. E. Waltz, Phys. Rev. Letters, 91, 045001, (2003)
[3] J. Candy and R. E. Waltz, J. Comput. Phys. **186**, 545 (2003).
[4] J. L. Luxon, Nucl. Fusion **42**, 614 (2002).
[5] G. R. McKee, et al., Rev. Sci. Instrum. **70**, 913 (1999).
[6] I. H. Hutchinson, *Principles of Plasma Diagnostics* (Cambridge University Press, 1987) pp. 152-155.
[7] G. Bekefi, *Radiation Processes in Plasmas* (John Wiley and Sons, NY, 1966) pp. 205-208, pp. 329-331.
[8] M. Bornatici, et al., Plasma Physics **23**, 1127 (1981).
[9] G. Cima, et al., Phys. Plasmas **2**, 720 (1995).
[10] C. Watts, et al., Nucl. Fusion **44**, 987 (2004).
[11] J. S. Bendat and A. G. Piersol, *Random Data: Analysis and Measurement Procedures,* (Wiley, New York, 1986).
[12] V. S. Udintsev, et al., Plasma Phys. Control. Fusion **48**, L33 (2006).
[13] S. Sattler, H. J. Hartfuss, and W.-A. Team, Phys. Rev. Lett. **72**, 653 (1994).
[14] B. H. Deng, et al., Phys. Plasmas **8**, 2163 (2001).
[15] V. S. Udintsev, et al., Tore Supra Team, A. Krämer-Flecken, Fusion Sci. and Technol. **50**, 508 (2006).
[16] L. G. J. Classen, et al., Proc. of 31st Euro. Physical Society Conf. on Plasma Physics, London, ECA Vol. 28G (2004) P1.121, and http://epsppd.epfl.ch/London/html/contents.htm#P1.
[17] C. Watts, Fusion Sci. and Technol. **52**, 176 (2007).
[18] H. M. Pickett, J. C. Hardy, J. Farhomand, IEEE Trans. Microwave Theory and Techniques **MTT-32**, 936 (1984).
[19] M. E. Austin and J. Lohr, Rev. Sci. Instrum. **74**, 157 (2003).
[20] A. P. Smirnov and R. W. Harvey, Bull. Am. Phys. Soc. **40**, 1837 (1995); A. P. Smirnov and R. W. Harvey, "The GENRAY Ray Tracing Code," CompX Report CompX-2000-01 (2001).
[21] M. Bomatici, et al., Nucl. Fusion **23**, 1153 (1983).
[22] S. Sattler and H. J. Hartfuss, Plasma Phys. Control. Fusion **35**, 1285 (1993).
[23] R. V. Bravenec and W. M. Nevins, Rev. Sci. Instrum. **77**, 015101 (2006).
[24] C. Holland, private communication (2008).
[25] M. W. Shafer, R. J. Fonck, G. R. McKee, and D. J. Schlossberg, Rev. Sci. Instrum. **77**, 10F110 (2006).

[26] A. E. White, L. Schmitz, G. R. McKee, C. Holland, W. A. Peebles, T. A. Carter, M. W. Shafer, M. E. Austin, K. H. Burrell, J. Candy, J. C. DeBoo, E. J. Doyle, M. A. Makowski, R. Prater, T. L. Rhodes, G. M. Staebler, G. R. Tynan, R.E. Waltz, and G. Wang, Phys. Plasmas, 15, 056116, (2008).

[27] R. V. Bravenec and A. J. Wootton, Rev. Sci. Instrum. **88**, 802 (1995).

Acknowledgments

This research was supported by the US Department of Energy under DE-FG03-01ER54615, JP333701, DE-FG02-89ER53296, DE-FG02-07ER54917, DE-FG03-97ER54415, DE-FG02-89ER53296, DE-FC02-04ER54698, and DE-AC52-07NA27344. AEW and JCH were supported by appointments to the Fusion Energy Sciences Fellowship Program administered by Oak Ridge Institute for Science and Education under a contract between the US Department of Energy and the Oak Ridge Associated Universities. We thank the DIII-D team for their support of these experiments.